Boron-induced controlled synthesis of Co-nano particles over $B_x(CN)_y$ matrix for CO hydrogenation in aqueous media

Jyoti Gahtori [a,b], Gaje Singh [a,b], Jyotishman Kaishyop [a,b], Chandewar P. Rajendra [c], Chelsea L. Tucker [d], Tuhin S. Khan [a,b], Debaprasad Shee [c], Ankur Bordoloi [a,b,*]

[a] *Light and Stock Processing Division, CSIR-Indian Institute of Petroleum (IIP), Dehradun 248005, India*
[b] *Academy of Scientific and Innovative Research (AcSIR), Ghaziabad 201002, India*
[c] *Department of Chemical Engineering, Indian Institute of Technology Hyderabad, Telangana 502 284, India*
[d] *Engineering and Technology Institute Groningen, University of Groningen, Nijenborgh 4, 9747 AG Groningen, Netherlands*

ARTICLE INFO

ABSTRACT

$B_x(CN)_y$ supported cobalt nanoparticles have been synthesized by regulating the ratios of melamine and boric acid precursors. The carbonization step is adequate to generate the desired controlled-sized cobalt particles at an auto-reduced state that can eliminate the requirement of promotors (e.g., Pt) for the hydrogen-spillover effect. The presence of nitrogen in support enhances the dispersion of cobalt particles by providing sites for cobalt to nucleate and grow due to the interaction between cobalt and Π electrons from the sp^2-N center. Boron in the catalyst system significantly stabilizes the catalyst, thus improving its lifetime. However, the excess of boron promotes the aggregation of cobalt particles; therefore, optimal boron loading is preferable. Moreover, the binding energy calculation of Co_6 over the B-doped and undoped C_3N_4 surface computed through DFT studies shows a reduction in metal-support interaction with the addition of boron, which leads to the aggregation of the cobalt particles with high boron. Overall, the catalyst with the optimized boron and nitrogen-containing support-stabilized cobalt particles is highly efficient in the aqueous phase Fischer-Tropsch synthesis.

1. Introduction

Fischer-Tropsch synthesis (FTS) comprises the conversion of CO and H_2 (syngas) to a wide range of fuels and chemicals through heterogeneous catalysis, typically using iron and cobalt [1]. The activity of the cobalt-based catalysts within the Fischer-Tropsch synthesis depends on various factors, including the catalyst composition, choice of promoters, support materials, etc. [2]. The catalyst support material, in particular, plays a significant role in determining the dispersion and stability of cobalt metal particles during reaction [3]. Moreover, the supports provide mechanical and thermal strength to the metallic cobalt, which provides an active site in the FT synthesis [4–6].

Typical supports used on a commercial scale include SiO_2, TiO_2, and Al_2O_3 [7]. Recently, carbon [5,8,9] and zeolites have been investigated as potential support materials to stabilize cobalt nanoparticles in the highly dispersed state [10]. However, the effect of support on catalyst performance is still not fully understood [11]. Different factors that affect catalyst activity, reducibility, stability, and selectivity are particle size, surface area, porosity, electronic properties, metal-support interaction, surface acidity, and mass-transfer limitations [6,11,12]. For instance, a significant level of metal-support interactions (MSIs) between cobalt and oxidic supports [13] (due to their comparable ionic radii) can limit the reducibility of cobalt at lower temperatures, resulting in a lower metal surface area, and thus a lower number of active surface sites available for FTS.

Inert carbon materials such as carbon spheres (CSs), nanotubes (CNTs), and nanofibers (CNFs) have a high surface area and high thermal and mechanical strength and have lower metal-support interactions, thus are a favorable alternative to conventional oxidic supports for cobalt-based FTS catalyst [14–16]. The polarity of carbon supports can be tuned by using different hetero atoms such as boron, nitrogen, oxygen, phosphorous, and sulfur. It helps to stabilize the metal/metal-oxide particles in the support and introduces hydrophilicity to the material [17–19]. The addition of hetero atoms can also improve the surface polarity, regulate the metal-support interactions, and improve the dispersion of cobalt particles on the support surface [20,21].

One critical issue that arises while using carbon as a support material is the regeneration challenge after reaction-induced carbon deposition

(Boudouard reaction). In general, the regeneration typically occurs at a higher temperature in an oxygen-rich environment to remove deposited carbon. This process results in structural damage to carbon supports along with carbon leaching.

As an alternative, Boron-nitride (BN), a substance with a graphite-like structure, is a highly versatile inorganic material that has received a lot of attention due to its high thermal conductivity and stability, oxidation resistance, non-toxicity, etc. [22,23]. Boron-nitride has been shown to promote the high dispersion and stabilization of different active components [24,25]. However, the strong ionic character of BN makes it intrinsically inert, and hence, practical applications can be challenging. In contrast, the doped and defective BN obtained via chemical modifications is known to have enhanced chemical reactivity due to the increased possibility of the inclusion of metal in the BN matrix.

Zhang et al. [26] studied CO interaction differences between graphitic-BN (*g*-BN) and modified *g*-BN by DFT studies, where the modified *g*-BN possessed a higher affinity towards CO [26]. Similarly, Cao et al. [27] reported enhanced adsorption affinity of atomic hydrogen over the surface of hybrid BN-graphene compared to bulk graphene and BN. Furthermore, Wu et al. [23] showed that Fe-boron-carbon-nitrogen nanosheets (Fe-BCNNs) (prepared via one-pot thermal decomposition) exhibited higher activity and 8 times the CO conversion at 633 K when compared to Fe/BNNs prepared by incipient impregnation method. The encapsulation of Fe particles by BCNNs was thought to provide enhanced stability to Fe- nanoparticles at room temperature, which further prevents the deactivation of the catalyst under high reaction temperature. According to previous studies, boron-modified surfaces are more coke-resistance as boron atoms occupy carbon adsorption site to reduce the probability of coke formation, which can be helpful in designing the novel catalyst for FT synthesis [28,29].

While BCN heterostructure has been investigated as support within the Fischer-Tropsch synthesis [23,26,27], the suitability for aqueous phase Fischer-Tropsch synthesis (where partial pressures of water are high) has yet to be addressed. Operating the Fischer-Tropsch synthesis in an aqueous phase (as opposed to a wax slurry) has several advantages, such as easy separation of products from the reaction mixture, high dispersion of the catalyst particles in water in the reactor assembly, and the thermodynamic advantage of operating at lower temperatures (highly exothermic reaction) [30]. Furthermore, high partial pressures of water have been shown to enhance FT productivity. Co-adsorption of CO and water on the active sites may decrease the energy barrier for CO dissociation [31], and the presence of water has been reported to increase the concentration of monomeric species on the surface of the catalyst, leading to the formation of longer chain hydrocarbon (as opposed to methane) [32]. Few of our previous studies have shown that the different Co-loaded catalysts are highly active for CO hydrogenation at relatively lower temperatures in aqueous media and result in high C_{5+} hydrocarbon and significantly low amounts of CH_4 (<5%) [33–35].

Here, we present an investigation into the structure-activity relationship for a $B_x(CN)_y$-supported cobalt catalyst for aqueous phase Fischer-Tropsch synthesis. The $B_x(CN)_y$ support is synthesized using a mixture of melamine and boric acid as precursors with variable compositions to determine the structural impact of B, C, and N on the support material. Furthermore, the Co-loaded $B_x(CN)_y$ is tested for catalytic performance within aqueous-phase Fischer- Tropsch synthesis.

2. Experimental

2.1. Reagents and materials

All the reagents were obtained from Sigma Aldrich and used without further purification. Mixtures of gases (CO: H_2: N_2 = 1:2:1/3) were procured from Sigma Gas service, having purity up to 99.99%. Double-distilled water was used throughout this study.

2.2. Synthesis of catalyst

The catalysts were synthesized using a previously reported procedure with few modifications [36], where melamine and boric acid were used as the precursors for C—N and B, respectively. For the preparation of the support system, 0.1 M boric acid solution was prepared at 333 K. A specific amount of melamine was added to the solution, and the temperature was raised from 333 K to 373 K to obtain a clear solution. The solution was allowed to rotate at this temperature for 15 h, followed by drying at 363 K. The collected white solid was heated up to 1173 (ramp rate 5 K/min) for 4 h under the flowing N_2 at 50 mL/min. Various supports were prepared using different ratios of boric acid to melamine ranging from 1:1, 1:2, 1:4, 2:1, and 4:1.

The cobalt-loaded catalysts were prepared by adding cobalt precursor (cobalt nitrate hexahydrate) after 15 h rotation of the boric acid-melamine solution to keep a cobalt loading of 15 wt% and further kept for 10 h rotation. For ease of labeling, the different cobalt-loaded $B_x(CN)_y$ catalysts will be designated as B1M1, B1M2, B1M4, B2M1, and B4M1, corresponding to 1:1, 1:2, 1:4, 2:1, and 4:1 ratio of boric acid to melamine respectively. Scheme 1 represents the overall formation mechanism of Co@$B_x(CN)_y$ assembly.

2.3. Analytical measurements

XRD was performed at ambient temperature with a Proto Advance X-ray diffractometer with a Cu Kα radiation source having a Lynx eye high-speed strip detector. The patterns were recorded by 30 kV X-ray in the range of 2θ =5°-80° with 0.05° step size (dwell time = 1 s).

To analyze the pore architecture in the synthesized catalyst, N_2 adsorption-desorption isotherms were recorded using Micromeritics ASAP 2020. Before each measurement, the catalyst was degassed in a vacuum at 623 K.

The oxidation state of several active metals in the samples was measured using Thermo Scientific K-alpha X-ray photoelectron spectroscopy (XPS). To calibrate the binding energies of each element, the binding energy of C 1 s at 284.5 eV was used as a reference.

JEM 2100 was used to capture transmission electron microscopy (TEM) pictures (JEOL, Japan). A small amount of catalyst was suspended in ethanol and sonicated for 10–15 min. To capture the images, 2–3 drops were cast on a Cu grid supported by lacey carbon and allowed to dry.

Temperature programmed reduction (TPR) and CO-temperature programmed desorption (TPD) were carried out using Micromeritics Auto Chem II 2920 instrument. The catalyst was flushed with helium at 623 K for 2 h before being cooled to room temperature to get TPR signals. Then, 20% H_2 in He was fed over the catalyst while the temperature was raised linearly to 1173 K (heating rate: 10 K/min). A thermal conductivity detector (TCD) was used to analyze the change in the H_2 concentration in the effluent.

The CO-TPD signals were obtained in the same manner, as described above, by flushing with He first, followed by reduction at 623 K for 2 h using 20% H_2 in He. The surface of the catalyst was passivated by the flow of CO at 373 K, and the spectra were recorded in the range of 373–1100 K.

2.4. Catalytic activity test

The AFTS catalysts were tested in a high-pressure stainless steel 100 mL batch reactor (Parr instrument). Before the reaction, 0.5 g of catalyst was reduced for 2 h at 623 K with 20% H_2 in N_2 to reduce surface oxidized cobalt species. After reduction, the catalyst was dispersed in 40 mL of water before being added to the reactor. To avoid contaminants, the reactor was purged twice with reaction mixture gas (CO: H_2: N_2 = 1: 2: 1/3), then sealed and pressured to 3.0 MPa with reaction gas. At a stirring speed of 700 rpm, the CO hydrogenation productivity was measured at 453 K. Once the reaction temperature was reached, the
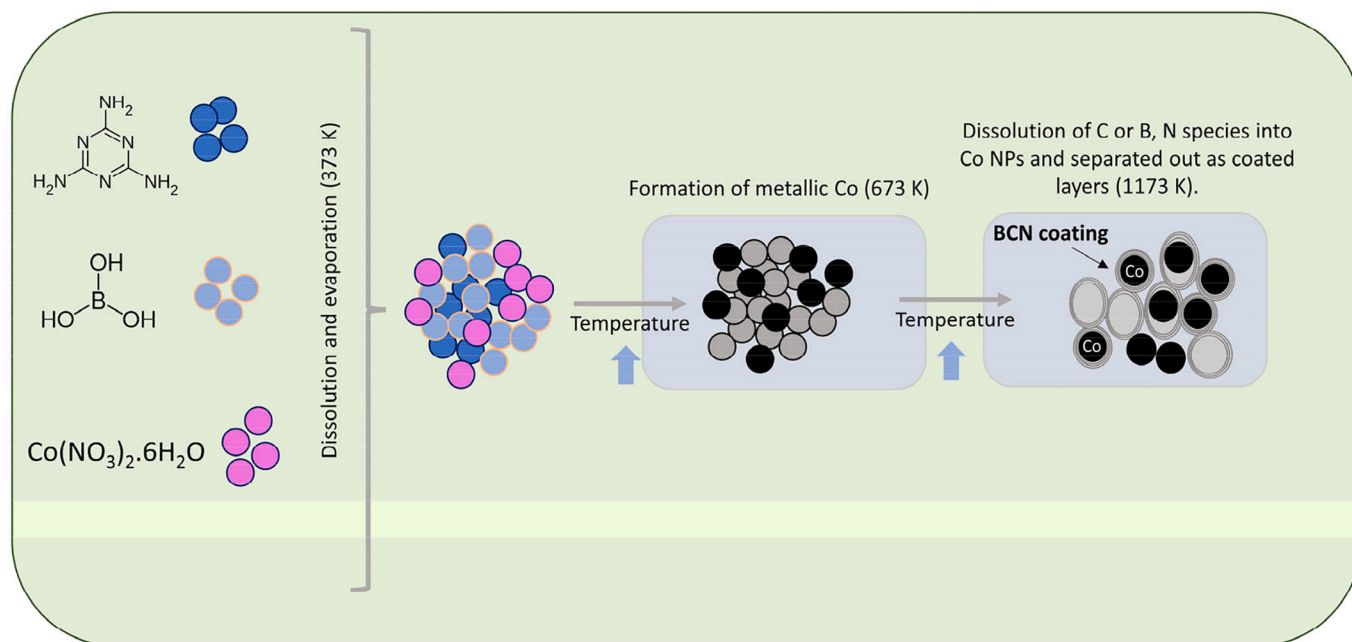
Scheme 1. The mechanism of formation of Co- $B_x(CN)_y$ catalyst assembly from different precursors [23].

reaction was carried out for 20 h for each catalyst.

When the reaction was completed, the reactor was cooled to room temperature, and the gaseous products were examined using an online gas analyzer (Agilent 7890B). A Molsieve 5A column was used to separate gasses H_2, CO_2, N_2, CH_4, CO, and C_2-C_3 which were subsequently quantified by a thermal conductivity detector (TCD). An HP-PONA column was used to separate gaseous C_4 hydrocarbons and evaluated using a flame ionization detector (FID). The liquid hydrocarbons were extracted from the autoclave by adding cyclohexane to the reaction mixture. The cyclohexane-containing organic layer was decanted, and the organic compounds were collected.

2.5. DFT calculation

All the experiments were performed using the spin-polarized CASTEP DFT method [37] as implemented in Material Studio 8 (Biovia, San Diego, USA) to understand the effect of boron doping on cobalt nanoparticle size for the $B_x(CN)_y$ supported Co-catalyst. The OTFG ultrasoft pseudopotentials were used for electron-core interactions, and the generalized gradient approximation (GGA-PBE) [38] was used to describe the exchange-correlation function. The electron wave function was expanded using plane waves with an energy cut-off of 396 eV. Convergence criteria for the DFT calculations were kept at 0.0002 eV, 0.05 eV/Å, and 0.002 Å concerning energy, force, and atom displacement, respectively. The k-points sampling of $1 \times 1 \times 1$ was used for all the calculations. The geometry of the C_3N_4 structure was obtained from the Materials Project database (mp-971,684) [39]. The C_3N_4 (CN) surface slab (Fig. S1a, SI) was created having two atomic layers, where the bottom layer was kept fixed to their bulk positions, whereas the top layer was allowed to relax during the geometry optimizations. The BCN surface was modelled by adding four B atoms at the defect site of the C_3N_4 surface slab (Fig. S1b, SI). A Co_6 nanocluster was made and grafted at the CN and BCN surfaces to model the Co-CN and Co-BCN catalyst surface.

3. Results and discussion

The crystallinity of the catalysts was investigated through XRD analysis and depicted in Fig. 1. The peak at 27.9^0 can be attributed to
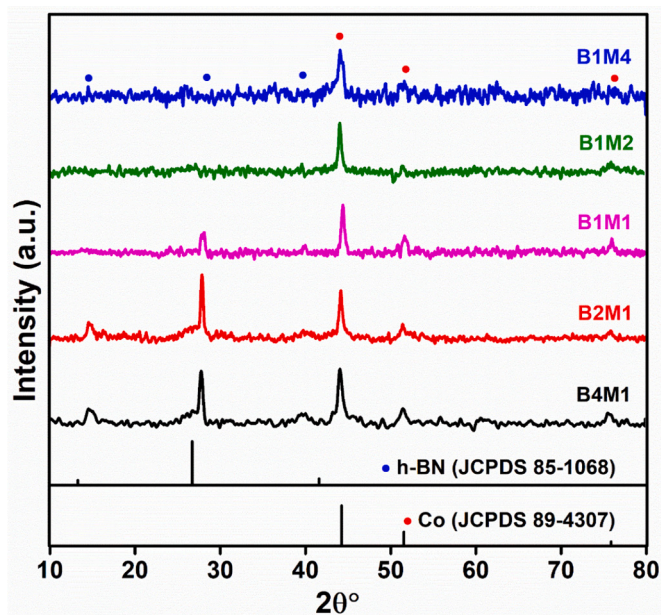

Fig. 1. XRD pattern of cobalt loaded $B_x(CN)_y$ prepared using different ratios of boric acid to melamine.

hexagonal boron nitride in the (002) plane, while a broad peak with very low intensity at $40–45^0$ can be correlated to the reflections due to (100) and (101) plane (JCPDS Card no. 85–1068) [40]. The peak at 14.8^0 in B2M1 and B4M1 can be associated with BN or carbon [23]. Depending upon the peak intensity, the nature of crystallinity was found to be different for each catalyst. These results show the formation of ternary B–C–N structure and successful boron doping in the C—N matrix. The increasing amount of melamine during the preparation of the catalyst results in the broadening of peaks in carbonized catalyst, accompanied by slight shifts to the lower angles. The formation of small-size NPs and increased dispersion may result in an enhanced broadening of the XRD peaks [41,42].

The N_2 adsorption-desorption isotherms for Co/$B_x(CN)_y$ are depicted

in Fig. 2, along with their surface areas mentioned in the corresponding figure. The BET surface area for cobalt-loaded catalysts was calculated to be in the range of 20 - 301 m^2/g. The sample code with B1M4 possesses a maximum surface area (301 m^2/g), whereas the B4M1 has the lowest surface area (20 m^2/g). The metal-support composites have a type IV isotherm and an H3 hysteresis loop, typical of a mesoporous structure. The bare $B_x(CN)_y$ (boron: melamine = 1:1) has a higher surface area (832 m^2/g) when compared to Co/ $B_x(CN)_y$ catalysts (< 300 m^2/g). It is possible that the cobalt particles clogged the microporous on the surface of the support, resulting in a significant drop in BET [23].

Fourier transform infrared spectroscopy (FTIR) further confirmed the chemical structure. Each catalyst showed varying peak intensity due to changes in the quantity of B, N, and C, which may impact the inner bonding in the interior of the catalyst in Fig. 3, the broad peak ranging from 3000 to 3700 cm^{-1} could be caused by residually bonded -NH or -OH groups [43]. The strong peak at 1390 cm^{-1} correlated with the in-plane B—N stretching vibration of h-BN, while the sharp peak at 770 cm^{-1} corresponds to the out-of-plane B–N–B bending vibrations. With raising the ratio of boric acid to melamine, the sharpness of their bands increases accordingly [36,40]. These two peaks are supposed to represent sp^2 bond fingerprints within h-BN, which is crucial proof of h-BN formation [44]. Additionally, two other small and broad peaks at 1620 cm^{-1} and 1060 cm^{-1} are associated with C—N and B—C adsorption bands respectively [45].

The surface chemical states of the fresh unreduced-metal loaded $B_x(CN)_y$ materials were investigated using XPS, shown in Fig. 4. As identified by XPS, the ratio of boric acid and melamine during synthesis
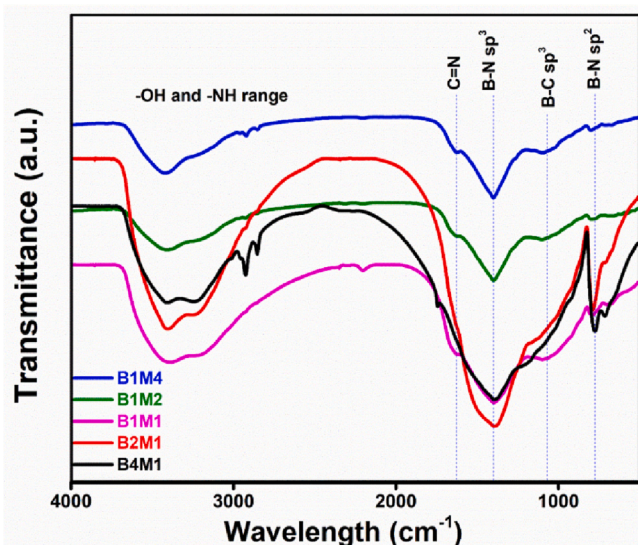

Fig. 3. FTIR plots for prepared support ($B_x(CN)_y$) using different ratio of boric acid to melamine.

appears to affect the different species in the catalyst. For Co 2p (Fig. 4a), the deconvoluted peak at 778.5 eV and 793.6 eV corresponds to metallic Co $2p_{3/2}$ and Co $2p_{1/2}$, while the peak at 781.5 eV and 796. 6 eV associated with Co^{2+} $2p_{3/2}$ and Co^{2+} $2p_{1/2}$ respectively [20]. The two
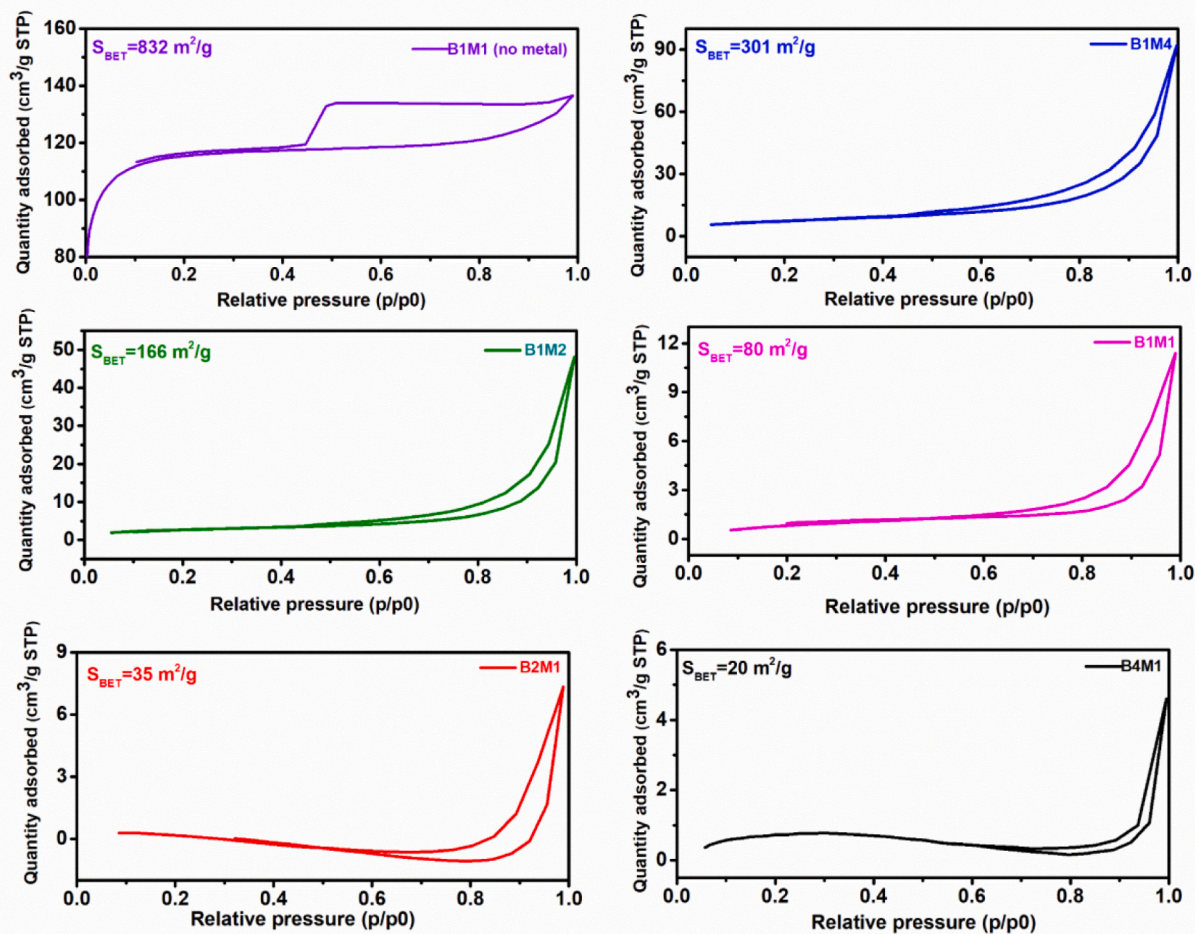

Fig. 2. N$_2$ adsorption-desorption plot for $B_x(CN)_y$ (Boric acid: melamine = 1:1) along with different cobalt-loaded $B_x(CN)_y$.

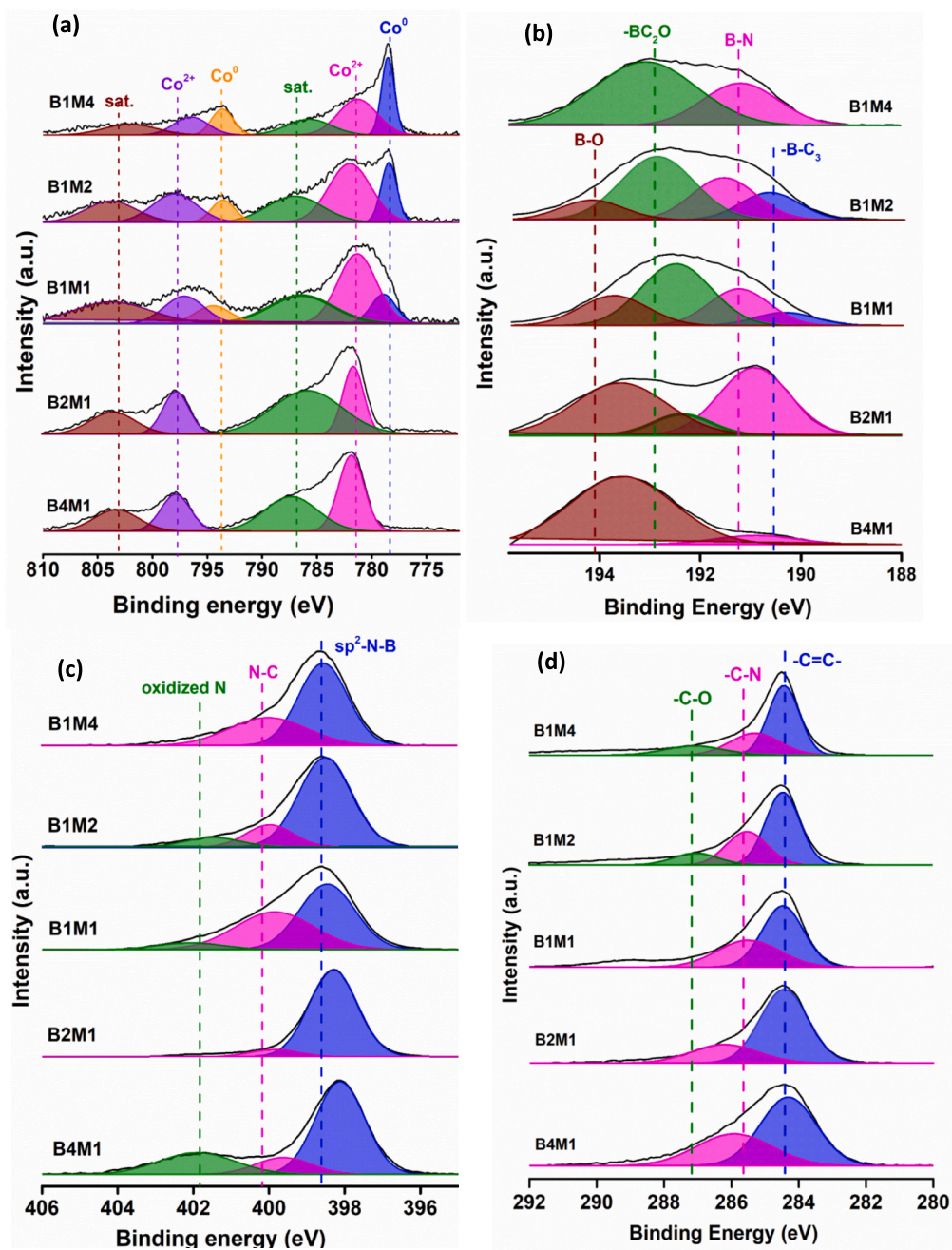**Fig. 4.** The XPS spectra for Co2p, B1s, N1s and C1s in freshly prepared catalysts.

satellite peaks at 786 eV and 803.5 eV could be generated due to the interaction of cobalt with oxygen or surface nitrogen [20,34]. In the case of B1M1, B1M2, and B1M4 catalysts, the cobalt was found to be in the mixed state of metallic and oxide form, while the other two catalysts, including B2M1 and B4M1, consist only of cobalt in its oxide state. This observation suggests the role of nitrogen in stabilizing the metallic cobalt on the surface of the support. There is a slight shifting of the peak position while moving from B1M4 to B4M1, which could be due to the change in the possible interaction of cobalt with the support.

The change in the electronic environment around Co while changing the amount of B and N/C in the catalyst can cause a change in its XPS spectra. During the carbonization process, the released gases, including H_2 and CO, behave as reducing agents for cobalt species. However, auto-oxidation of surface cobalt particles is typically unavoidable while handling the catalyst in a typical atmosphere. As a result, cobalt in a + 2-oxidation state has also been observed. The surface of the catalyst with a

high amount of nitrogen (B1M4) is richest with metallic cobalt. It could be possible due to the stabilization caused by Π electrons of sp^2-N from the support. Additionally, the nitrogen-containing functional groups of support can accelerate the conversion of Co_3O_4 to metallic Co and prevent it from aggregating [46]. Here, the effect of reducing gases on the surface cobalt particles was almost negligible in the case of the catalyst prepared using a high amount of boric acid (B2M1 and B4M1), and the surface of the catalysts was observed to be rich with divalent cobalt. Although the XRD patterns demonstrated that the bulk of the catalyst consists of metallic cobalt, the surface has been decorated with a mixed assembly of divalent cobalt and metallic cobalt. The XPS spectra of B1s (Fig. 4b) are quite complex. The peak at 193 eV corresponds to -BC$_2$O, while the peak at 191.2 eV is associated with the B—N bond [47].

A peak at 194 eV corresponds to the B—O bond. The maximum peak intensity for B—O spectra was observed in the case of B4M1 catalysts, which shows that a significant amount of boron is present as boron oxide

in the catalysts even after carbonizing at 1173 K. The red shift in the peaks was observed while moving from B1M4 to the B4M1 catalyst, possibly due to different bonding originating during carbonization.

Fig. 4c represents the XPS spectra for N1s species present in the catalyst. The peaks at 398.2 and 399.8 eV correspond to pyridinic-N and pyrrolic-N, respectively, while a peak at 402.4 eV can be correlated to the oxidic [34,47]. The peak area for N1s species in each catalyst shows that pyridinic nitrogen is the predominant species. According to reports,

the N- species are thought to act as essential electron donors during FT synthesis to enhance the CO adsorption–dissociation process and are in charge of adjusting the selectivity of the resulting products [13]. Similarly, the XPS spectra for C1s (Fig. 4d) species show the presence of C=C, C—B, and C—O bonds corresponding to the peak that appeared at 284.4, 285.6, and 287.1 eV, respectively [42]. The TEM and SEM analysis were used to examine the morphology and structure of the prepared catalyst. The TEM images, along with the cobalt particle size
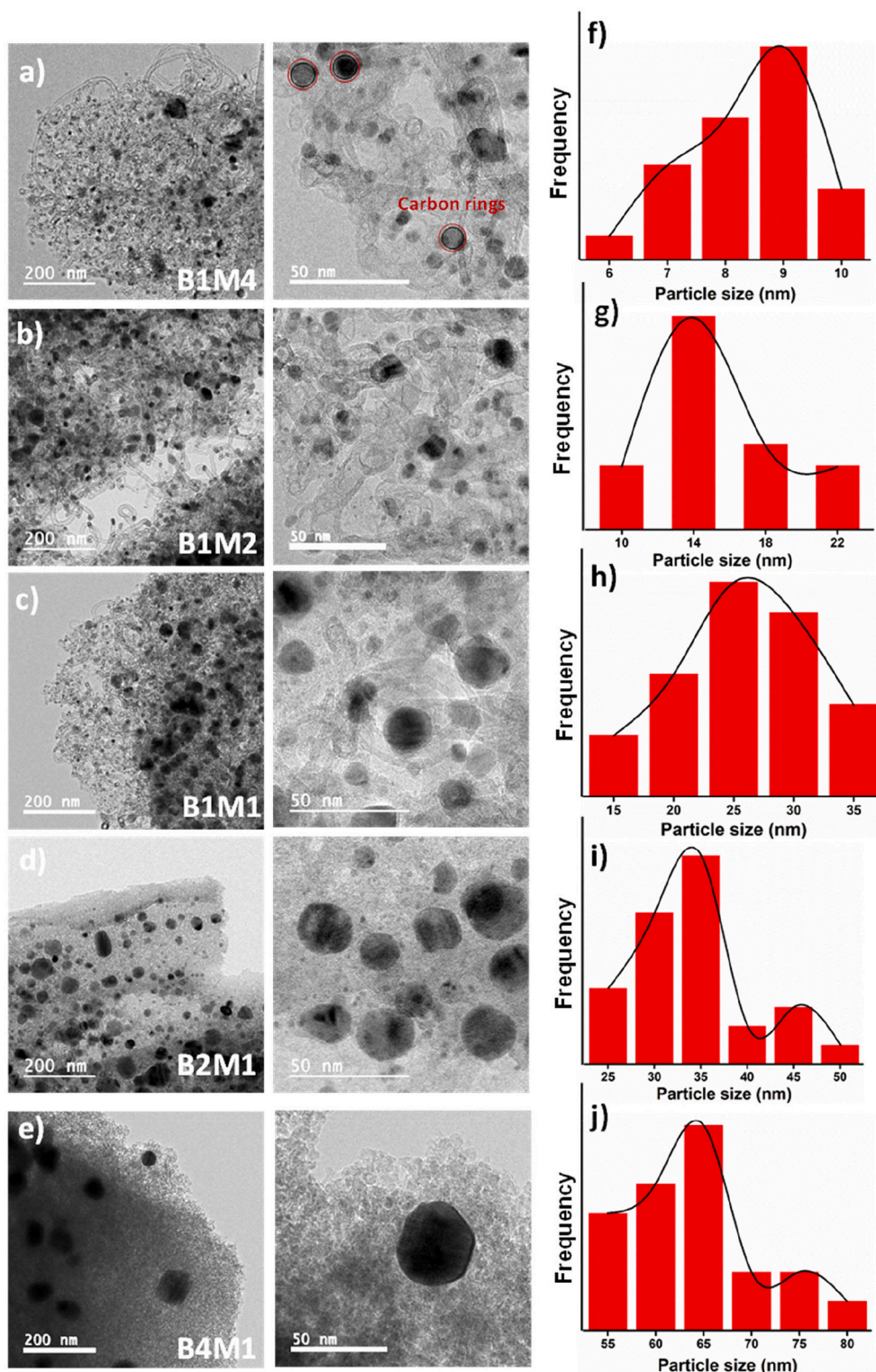

Fig. 5. TEM images for Co loaded on different $B_x(CN)y$ supports with the corresponding particle size distribution.

distribution, are depicted in Fig. 5. The cobalt nanoparticles over $B_x(CN)_y$ are evenly dispersed; however, there is a visible increase in the particle size with increasing amounts of boric acid. Additionally, the formation of CNTs was observed in few of the catalysts (B1M4, B1M2 and B1M1), having a large amount of C and N, which is likely due to the presence of cobalt as a radical centre to grow nanotubes in the catalyst. In the case of the B1M4 catalyst, the average particle size of cobalt was calculated to be 8–10 nm, which increases with decreasing amount of nitrogen in the support matrix. The average particle size of cobalt in the case of B4M1 was found to be >60 nm. Due to the strong interaction between cobalt and Π electrons, it is assumed that cobalt preferentially aggregates on sp^2-type nitrogen sites to nucleate and grow. It suggests that nitrogen in the carbon support aids in the dispersion and immobilization of cobalt species. The cage-like structure of carbon encapsulating around the cobalt particles (Fig. 5a) can retard the sintering of the particles, their oxidation, and leaching during the reaction. The presuming effect of water on the small-size cobalt particles from our previous study [34] led us to limit the amount of melamine to the taken value. The further increment in melamine (beyond B1M4) can decrease the average size of cobalt particles below 6 nm, affecting the catalytic activity and selectivity of the required product.

DFT studies further corroborated the structural changes in the cobalt-$B_x(CN)_y$ assembly. Fig. 6(a-b) represents the DFT-optimized geometry of Co_6-C_3N_4, where it has been observed that the Co_6 nanocluster preferentially adsorbs at the defect site of the CN surface, forming a total of five bonds with the N-atoms. The Co—N bond lengths were 2.04 Å, 2.19 Å, 2.04 Å, 2.1 Å, and 2.0 Å, respectively. The Co_6 nanocluster binds strongly to the CN defect site with a binding energy of −4.73 eV, indicating metal-support solid interaction. The adsorption geometry of Co_6 at the C_3N_4 surface indicates that the Co_6 nanocluster was embedded into the C_3N_4 defect site, which will hinder the diffusion of these nanoclusters out of the C_3N_4 surface defect site. The DFT-optimized geometry of Co_6 adsorbed at the B-doped C_3N_4 surface is shown in Fig. 6(c-d).

In the B-doped C_3N_4 surface, the Co_6 nanocluster adsorbs on top at the already adsorbed B, as shown in Fig. 6(c). The Co—B bonds distance was measured to be 2.0 Å, and the binding energy of Co_6 over the B-doped C_3N_4 surface was computed to be −4.19 eV, which was ~0.54 eV lower than that of the binding energy of Co_6 over the undoped- C_3N_4 surface, indicating a reduction in metal-support interaction. The higher metal-support interaction facilitates the stacking of Co nanoparticles on the surface of C_3N_4. In contrast, when B was doped on the C_3N_4 surface, comparatively weaker metal-support interaction led to agglomeration of the Co metal nanoclusters, resulting in an increase in the particle size in the Co- $B_x(CN)_y$ catalyst as also observed experimentally in TEM analysis (Fig. 5). The SEM images for B1M4 and B4M1 catalysts are depicted in Fig. 7, showing the rod-like morphology of $B_x(CN)_y$ supports. The H_2-TPR plots of Co/CoOx-$B_x(CN)_y$ catalysts are depicted in Fig. 8, and the amount of absorbed hydrogen is summarized in Table 1. Although the amount of absorbed hydrogen is relatively small (probably contributing only to the reduction of surface cobalt oxide species), it can help understand the nature and the interaction of the cobalt with the support of the different catalysts.

A total of four regions are observed in the H_2 consumption curve, of which one can be assigned to the decomposition of residual cobalt nitrate [48]. At the same time, the other peak area can be correlated to the reduction of different cobalt species present in the catalyst.

Since the auto-oxidation of surface cobalt species may generate CoOx, here, the region I can be correlated with the reduction of auto-oxidized CoOx supported on the surface of the support. In contrast, region II shows the reduction of CoOx particles, which strongly interacted with the support [49]. Region III, relatively at a very high temperature, can be linked with the reduction of large CoOx particles, which do not interact with the support [49]. Since the area under peak III is highest in the case of the B4M1 catalyst, it can be correlated to the reduction of large isolated cobalt oxide particles, which are challenging to reduce at low temperatures due to their size.

The five samples have different reduction profiles, indicating that the interaction of cobalt particles with the support is different in each catalyst. The highest peak area under the curve in region III was observed with increasing the amount of boron in the catalyst. In general, nitrogen in the catalysts system acts as the nucleation site for cobalt to grow by strong interaction between cobalt and Π electrons and immobilizing it on the surface of the catalysts [50]. However, the low amount of N in the catalysts system decreases the interaction of cobalt with the support, which may lead to significant and isolated cobalt particles. The observation from TEM images and the TPR plots show that the large growing cobalt particles on the surface of catalysts having a low amount of nitrogen are challenging to reduce at low temperatures, which significantly affects the catalytic activity during AFTS.

The CO-TPD plots for all the prepared catalysts are depicted in Fig. 9a, and the quantitative value is summarized in Table 1.

This study aimed to analyze the adsorption of CO on the surface of the catalyst, which might be affected due to the presence of boron and nitrogen in the system.

The presence of excess boron on the catalyst surface is expected to withdraw the electron density from the active cobalt center due to its acidic nature and hence decrease the adsorption of CO on the surface. In contrast, as an electron donor atom, nitrogen is expected to increase the electron density on the cobalt atom and facilitate the adsorption of CO on the catalyst surface [51]. In Fig. 9a, the first two desorption peaks appear near 400–700 K and 700–900 K, while the high-temperature peak appears at 900–1100 K. In the case of the B4M1 catalyst, the adsorption of CO on the surface of the catalyst was very low, which can be ascribed the presence of excess boron on the catalyst surface, which may withdraw electron density from cobalt and make the adsorption of CO on the surface of the catalysts as highly unfavorable. Contrary to B4M1, in the case of the B1M4 catalyst, the adsorption of CO on the surface was highly favorable (Fig. 9a), which is ascribed to the presence of nitrogen in the catalyst system, which increases the electron density of the cobalt system and thus favors the interaction of Co—C-O bond
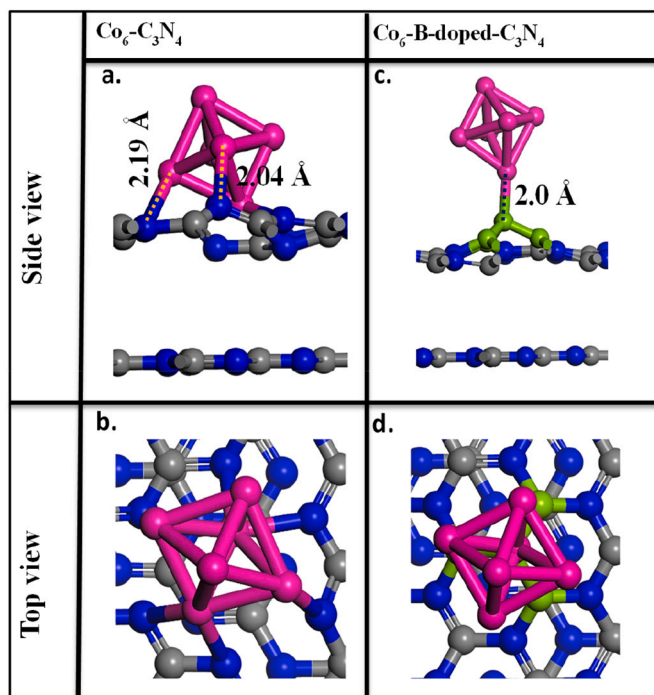

Fig. 6. Optimized geometry of Co_6 adsorbed C_3N_4 (a, b) and B-doped C_3N_4 (c, d). Color code: C (grey), N (blue), Co (pink), and B (green). (For interpretation of the references to color in this figure legend, the reader is referred to the web version of this article.)
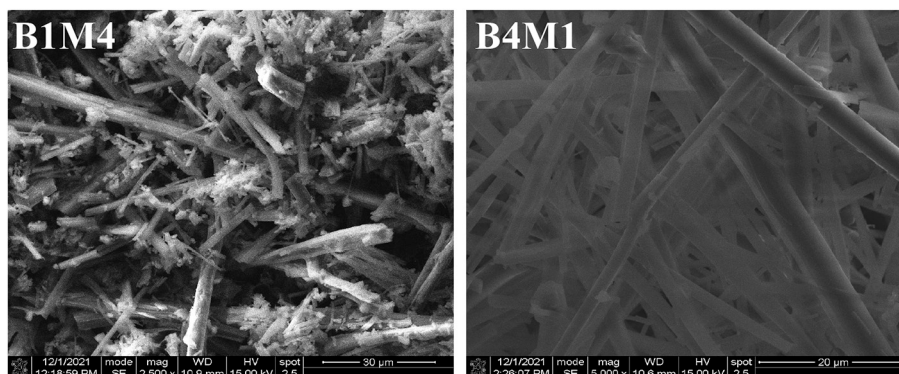
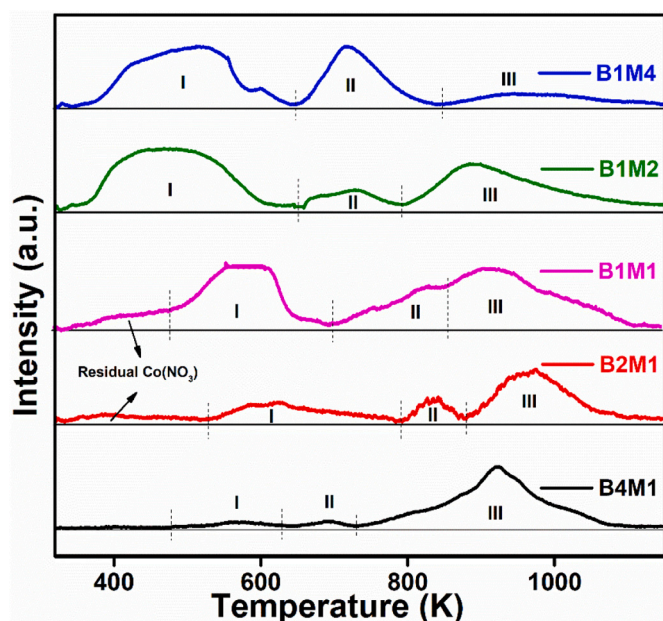**Fig. 7.** SEM images for B1M4 and B4M1 support.

Fig. 8. H_2-TPR profile for different prepared catalysts.

Table 1
CO uptake determined from TPD studies and H_2 consumption.

S. No.	Catalyst	Total CO uptake (mmol/g)	Total H_2 consumption (mmol/g)
1	B1M4	2.60	0.075
2	B1M2	1.14	0.065
3	B1M1	0.87	0.035
4	B2M1	0.44	0.021
5	B4M1	0.11	0.014

during the reaction.

The in-situ DRIFTS studies were recorded for each catalyst at 453 K with the mixture of CO, H_2, and N_2 (1:2:1/3) after 5 h. The corresponding spectra are depicted in Fig. 9b. A broad band at 2067 cm^{-1} corresponding to a typical CO linear and bridging over metal Co particles [52,53] was observed in the B1M4 catalyst, with the relatively low intensity in the case of the B1M2 catalyst. However, in the remaining catalyst, this band disappears. A low-intensity band at 2119 cm^{-1} can be assigned to the physically adsorbed CO [54].

The stability of the prepared catalysts was analyzed using thermogravimetric analysis in the presence of oxygen. In general, the deposited carbon after the FTS reaction over the surface of the catalyst is removed by a simple calcination method operated below 800 K [23]. However,

the method is limited for carbon-based support because the oxidation of the surface carbon from the support makes the catalyst unstable during regeneration.

Fig. 10a depicts the TGA curve for the different boron-doped catalysts. It shows the stability of the catalysts up to 800 K and beyond 1100 K in a few of the catalysts in the presence of oxygen, which can help regenerate and reuse the catalyst. The presence of boron in the support system was found to provide stability against oxidation. As a result, it can be an excellent option for using it as an encapsulating material, especially in the FTS reaction. In contrast, Fig. 10b shows the TGA plot for cobalt-loaded (CN)x catalysts prepared using melamine. Here the significant weight loss was observed at 500–600 K due to the oxidation of carbon from the support. Hence the regeneration of the catalyst requires a stable and oxidation-resistant catalyst.

The catalytic activity and the product selectivity using different Co-loaded catalysts that are composed of different compositions of boron, carbon, and nitrogen were analyzed after 20 h reaction in an aqueous phase batch reactor at 453 K and 3 MPa with a reaction gas mixture (CO: H_2: N_2 = 1: 2: 1/3). Before loading the catalyst in the reactor system, the catalyst was reduced at 623 K for 2 h using 20% H_2 in He atmosphere. Different parameters, including the effect of the volume of water in the reactor and the reaction time, were also studied using the B1M4 catalyst having the highest productivity among all the catalysts. These results are shown in Fig. 11.

The effect of boron and nitrogen within AFTS was studied by preparing five additional support using different ratios of boric acid to 3 MPa (CO: H_2: N_2 = 1:2: 1/3) with 40 mL water in the reactor using 0.4 g of catalyst. The CO conversion decreased with an increasing amount of boron in the catalyst (Fig. 11a).

The CO conversion was 93% for B1M4 catalysts, as opposed to 56% in the case of B4M1 catalysts after 20 h. The TEM images of B1M4 show that the cobalt particles are smaller and highly dispersed over the surface of the catalysts and, thus, likely to provide a more significant number of active sites. Moreover, it could be speculated that oxidation of the cobalt particles by water is limited due to encapsulation caused by carbon around the cobalt particles in the case of B1M4 and B1M2. The particle size of cobalt increases with decreasing nitrogen and.

increasing boron, possibly due to the aggregation of the particles. Furthermore, XPS indicated that the surface of the boron-rich catalysts has high concentrations of cobalt oxide, and H_2-TPR showed that cobalt on these supports, including B2M1 and B4M1, is challenging to reduce. So, the combined effect of larger crystallite size, sluggish reduction, and high concentrations of cobalt oxide for the boron-rich catalysts likely caused the lower conversions within the Fischer-Tropsch system.

Hence, B1M4 (which achieved the highest CO conversion) was further used to study the effect of the amount of water, time, and support material. The effect of water in the reactor system was studied by changing the volume of water from 10 mL to 60 mL while maintaining the same reaction conditions as stated in the previous section. The CO
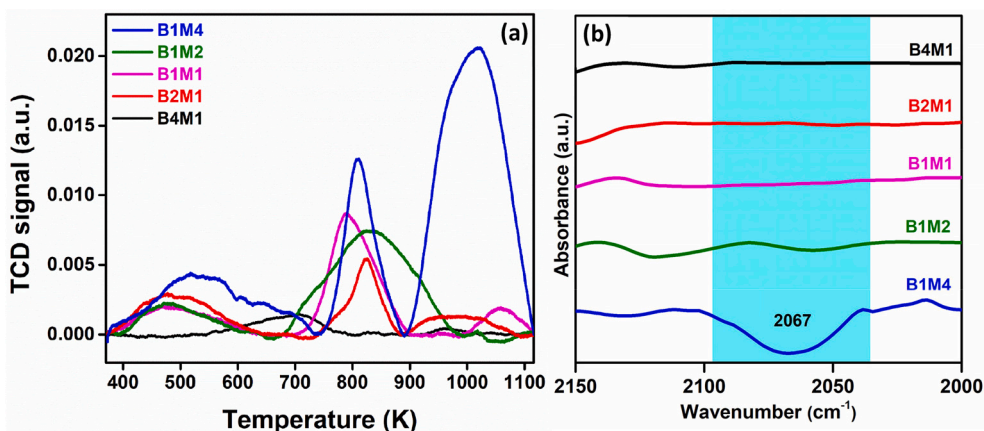
Fig. 9. **a)** CO-TPD plots and **b)** in-situ DRIFT studies for different Co-loaded $B_x(CN)_y$ catalyst.
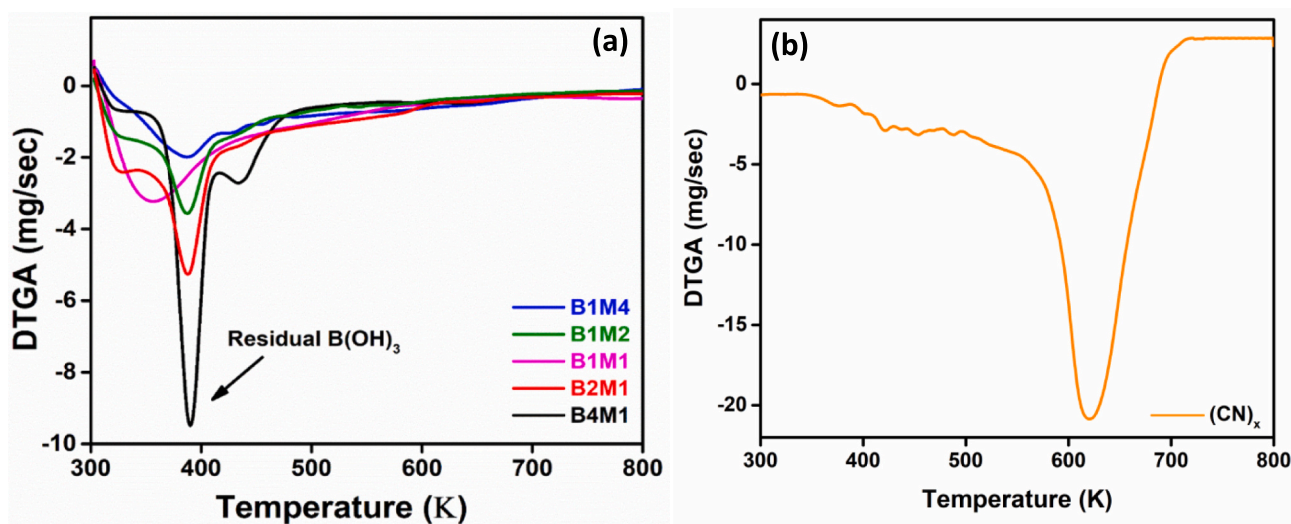

Fig. 10. TGA of a) different prepared catalysts in the presence of oxygen; b) for CN*x*.

conversion, depicted in Fig. 11b, was increased from 45% to 93% by increasing the amount of water from 10 mL to 40 mL; however, further increasing the volume of water from 40 to 50 mL, the CO conversion became almost constant. The effect of water on CO conversion is well explained computationally by Bertole et al. [32] In Fischer–Tropsch synthesis, adding a limited amount of water to the feed improves catalyst activity, where water is thought to increase CO activation, resulting in a more significant concentration of propagated monomers [55]. It is also reported to cause the selectivity towards methane to decrease with the increased partial pressure of water [56–58], an observation confirmed in our study.

Excess water can cause activity loss and a rapid deactivation rate, reversible or irreversible, depending on the catalyst formulation [18]. Likely, the addition of 40–50 mL of water in the reactor caused a positive effect on the CO conversion, while a further increase in the volume of water decreased the CO conversion.

Fig. 11c shows the effect of reaction time on the CO conversion and selectivity towards different products. Increasing the reaction time from 1 h to 5 h, 10 h, 15 h, and 20 h resulted in an increase in CO conversion from 22% to 48%, 67%, 81%, and 93%. The selectivity of methane was initially 0.6 -C%, which increased to 4.4 -C% after 20 h, which is low compared to the Fischer-Tropsch batch systems using cobalt-based catalysts [59]. However, the selectivity of the CO_2 was elevated compared to typical FT synthesis, which could relate to the obtained from TPR

results presence of water in the system, which may facilitate water gas shift reaction.

The recyclability experiments for the B1M4 catalyst were also conducted (Fig. S3), which shows that the catalyst is recyclable up to 5 times without any significant loss in its activity. The material characterizations of spent B1M4 catalyst are depicted in the supplementary information, including XRD, TEM and XPS spectra. The XRD peaks (Fig. S4) show that the cobalt is present in a metallic state after the reaction. The TEM images show no accumulation of cobalt particles in the spent catalyst (Fig. S5). The XPS spectra (Fig. S6b) of spent B1M4 shows the presence of both metallic cobalt and CoO_x on the surface of catalyst with the slight broadening of peaks, which could be related to the enhanced interaction of CoO_x particles with the support under reaction conditions. A comparative study with different catalysts, including 15 wt% cobalt-loaded commercial activated carbon (AC), carbon nanotubes (CNTs), boron nitride (BN*x*), and self-synthesized (CN)*x* are presented in Fig. 11d. The metal-loaded AC and CNTs showed very low CO conversion, i.e., 25% and 31%, respectively, which can be related to their non-polar nature, which results in low stabilization of metal particles on the surface of the support and it can lead to leaching of metal particles in water. Moreover, due to the non-polarity of the support, the poor dispersion of the catalyst particles can eradicate the effect of using water as a reaction medium.

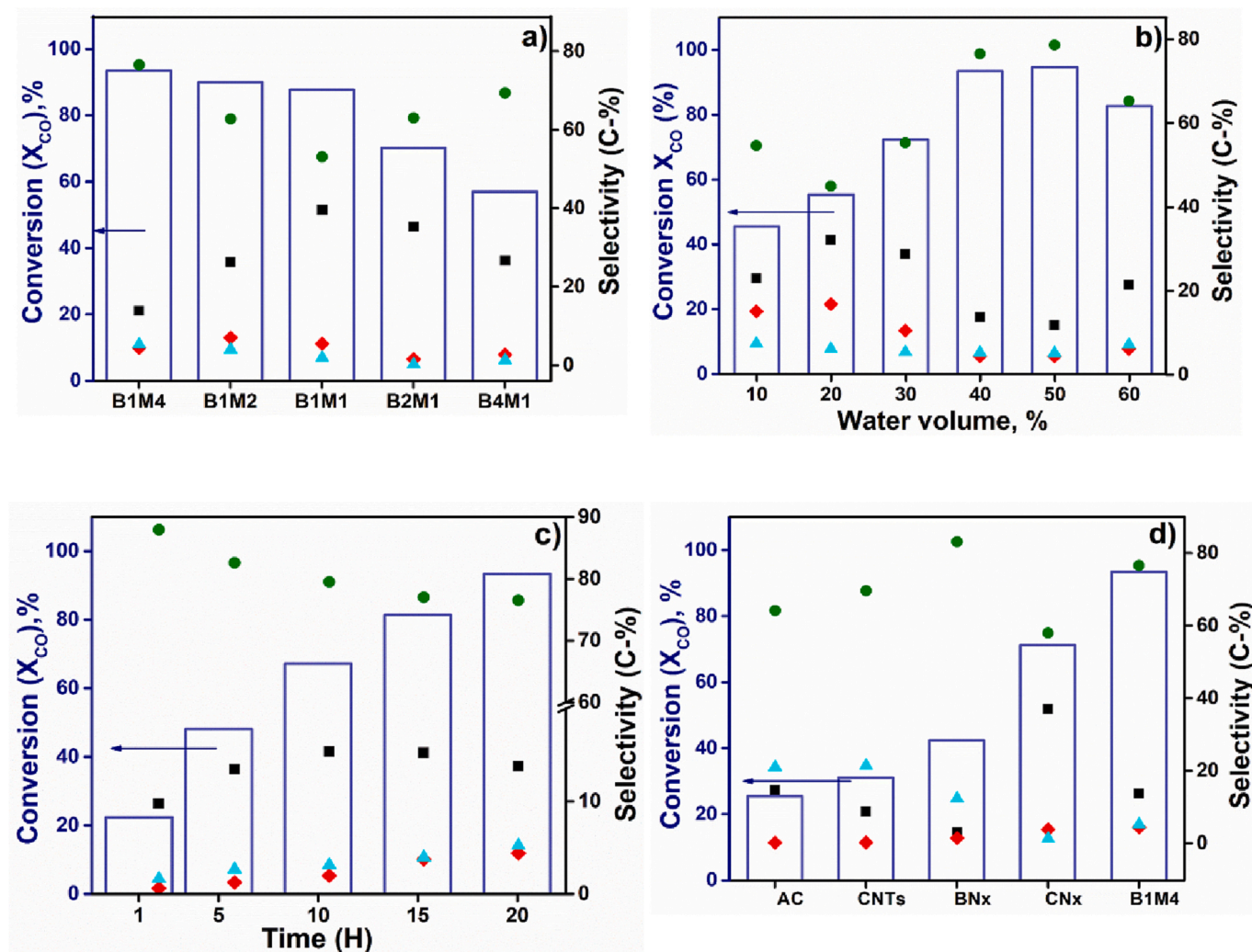The (BN)*x* is considered a favorable support material for cobalt-based

Fig. 11. Conversion (−) and selectivity (■ CO_2, ◆ CH_4, ▲ C_2-C_4 and ● C_{5+}) for a) different prepared catalysts; b) influence of water in reactor system; c) effect of reaction time; and d) comparative study with different catalysts.

Fischer-Tropsch synthesis due to its high stability and resistance to oxidation. However, its rigid structure makes metal deposition difficult and thus requires the chemical defects generated by carbon in the structure to accommodate the metal particles. Chen et al. [36] showed that incorporating C in the h-BN enhances the CO_2 adsorption capacity. In our study, the metal deposited on $(BN)x$ shows low CO conversion (42%) compared to our prepared catalysts.

Similarly, the metal-loaded $(CN)x$, prepared using melamine as a source, shows only 71% CO conversion. The low CO conversion compared to B$(CN)x$ can be related to the strong integral Lewis-basic interaction effect of B and N, as explained earlier. The catalyst prepared using boric acid to melamine in the ratio of 1:4 shows the best performance with a CO conversion of 93% and a 76% selectivity towards C_{5+} hydrocarbons.

The reproducibility studies of the B1M4 catalyst have been conducted by performing the reaction 4 times (4 runs). A fresh catalyst is used in each run of the reaction. The data in Table 2 indicate the comparable performance of the B1M4 catalyst in all 4 runs. Further, the extent of standard deviation in data has been calculated and depicted in Fig. S2. The error bars (in Fig. S2) represent the standard error of the average values. The results from these studies support that the B1M4 catalyst exhibits comparable catalytic performance within the considerable limits of standard deviation. However, the possibility that such negligible variations are simply the results of instrument and procedure

errors.

Table 2

The representation of deviation in the FTS results for the B1M4 catalyst (graphically presented in Fig. S2).

	Repeat runs				Average	Standard Deviation
	Batch 1	Batch 2	Batch 3	Batch 4		
Conversion	93.4	91.6	93.7	90.8	92.4	1.4
CO_2	13.8	13.2	15.6	17.4	14.9	1.9
CH_4	4.4	6.4	6.2	4.4	5.5	0.9
C_2-C_4	5.2	0.89	3.16	2.07	2.8	1.8
C_{5+}	76.6	79.5	75.0	76.2	76.8	1.9

4. Conclusions

This work demonstrates a straightforward method to prepare highly stable and dispersed cobalt-loaded $B_x(CN)_y$ catalysts for aqueous phase Fischer Tropsch synthesis. Among the different series of catalysts, the catalysts comprise of 1:4 ratio of boric acid, and melamine (B1M4) shows a high CO conversion of 93% with 76.5% C_{5+} hydrocarbon selectivity. The catalyst exhibits relatively low methane formation, likely due to the aqueous phase (high water partial pressures). The highly dispersed cobalt particles and their stabilization from water by

carbon forming an outer coverage around the particles are the probable keys to such high CO conversion. The excess amount of boron in the support can lead to low CO adsorption due to its highly electron-deficient nature. In contrast, the absence of boron affects the stability of the catalyst and the catalytic activity. The presence of boron provides stability by resisting the support from oxidation during regeneration. Its significant amount also enhances the CO conversion by Lewis-acid base interaction between O atom from CO with boron from the support. From DFT results, the binding energy of Co_6 over the B-doped C_3N_4 surface was computed to be -4.19 eV, which was ~ 0.54 eV lower than that of the binding energy of Co_6 over the undoped- C_3N_4 surface, indicating a reduction in metal-support interaction and bigger particles of Co. Hence, the reported catalyst with the optimized loading of B and C—N is highly efficient in achieving high CO conversion at relatively low temperatures and highly stable against oxidation.

Credits author statement

- **Jyoti Gahtori:** Data curation, Formal analysis, Investigation, Methodology, Writing-original draft.
- **Gaje Singh:** Data curation, Validation, Visualization.
- **Jyotishman Kaishyop:** Data curation, Formal analysis, Investigation, Methodology.
- **Chandewar P. Rajendra:** Investigation, Methodology.
- **Chelsea** L. **Tucker:** Writing-review, editing.
- **Tuhin S. Khan:** Software, Methodology.
- **Debaprasad Shee:** Data curation, Formal analysis, Validation, Visualization.
- **Ankur Bordoloi:** Conceptualization, Funding acquisition, Project administration, Resources, Supervision, Validation, Visualization, Writing – review & editing.

Declaration of Competing Interest

"There are no conflicts to declare."

Data availability

Data will be made available on request.

Acknowledgments

Appendix A. Supplementary data

Supplementary data to this article can be found online at https://doi.org/10.1016/j.fuproc.2023.107719.

References

[1] I.C. ten Have, B.M. Weckhuysen, The active phase in cobalt-based Fischer-Tropsch synthesis, Chem Catal. 1 (2021) 339–363, https://doi.org/10.1016/j.checat.2021.05.011.

[2] G. Jacobs, T.K. Das, Y. Zhang, J. Li, G. Racoillet, B.H. Davis, Fischer-Tropsch synthesis: support, loading, and promoter effects on the reducibility of cobalt catalysts, Appl. Catal. A Gen. 233 (2002) 263–281, https://doi.org/10.1016/S0926-860X(02)00195-3.

[3] R. Munirathinam, D. Pham Minh, A. Nzihou, Effect of the support and its Surface modifications in Cobalt-based Fischer-Tropsch Synthesis, Ind. Eng. Chem. Res. 57 (2018) 16137–16161, https://doi.org/10.1021/acs.iecr.8b03850.

[4] N. Fischer, E. van Steen, M. Claeys, Structure sensitivity of the Fischer–Tropsch activity and selectivity on alumina supported cobalt catalysts, J. Catal. 299 (2013) 67–80, https://doi.org/10.1016/j.jcat.2012.11.013.

[5] G.L. Bezemer, J.H. Bitter, H.P. Kuipers, H. Oosterbeek, J.E. Holewijn, X. Xu, F. Kapteijn, A.J. van Dillen, K.P. de Jong, Cobalt particle size effects in the Fischer-Tropsch reaction studied with carbon nanofiber supported catalysts, J. Am. Chem. Soc. 128 (2006) 3956–3964, https://doi.org/10.1021/ja058282w.

[6] E. Iglesia, Design, synthesis, and use of cobalt-based Fischer-Tropsch synthesis catalysts, Appl. Catal. A Gen. 161 (1997) 59–78, https://doi.org/10.1016/S0926-860X(97)00186-5.

[7] M.E. Dry, The Fischer-Tropsch process: 1950-2000, Catal. Today 71 (2002) 227–241.

[8] G.L. Bezemer, P.B. Radstake, V. Koot, A.J. Van Dillen, J.W. Geus, K.P. De Jong, Preparation of Fischer-Tropsch cobalt catalysts supported on carbon nanofibers and silica using homogeneous deposition-precipitation, J. Catal. 237 (2006) 291–302, https://doi.org/10.1016/j.jcat.2005.11.015.

[9] M. Trépanier, A. Tavasoli, A.K. Dalai, N. Abatzoglou, Co, Ru and K loadings effects on the activity and selectivity of carbon nanotubes supported cobalt catalyst in Fischer-Tropsch synthesis, Appl. Catal. A Gen. 353 (2009) 193–202, https://doi.org/10.1016/j.apcata.2008.10.061.

[10] X. Peng, K. Cheng, J. Kang, B. Gu, X. Yu, Q. Zhang, Y. Wang, Impact of Hydrogenolysis on the Selectivity of the Fischer-Tropsch synthesis: diesel fuel production over mesoporous zeolite-Y-supported cobalt nanoparticles, Angew. Chem. Int. Ed. 54 (15) (2018) 4553–4556, https://doi.org/10.1002/anie.201411708.

[11] J. Liu, D. Wang, J.F. Chen, Y. Zhang, Cobalt nanoparticles imbedded into zeolite crystals: a tailor-made catalyst for one-step synthesis of gasoline from syngas, Int. J. Hydrog. Energy 4 (2016) 21965–21978, https://doi.org/10.1016/j.ijhydene.2016.10.004.

[12] A.Y. Khodakov, W. Chu, P. Fongarland, Advances in the development of novel cobalt Fischer-Tropsch catalysts for synthesis of long-chain hydrocarbons and clean fuels, Chem. Rev. 107 (2007) 1692–1744, https://doi.org/10.1021/cr050972v.

[13] L.M. van Koppen, A. Iulian Dugulan, G. Leendert Bezemer, E.J.M. Hensen, Sintering and carbidization under simulated high conversion on a cobalt-based Fischer-Tropsch catalyst; manganese oxide as a structural promotor, J. Catal. 413 (2022) 106–118, https://doi.org/10.1016/j.jcat.2022.06.020.

[14] Q. Cheng, N. Zhao, S. Lyu, Y. Tian, F. Gao, L. Dong, Z. Jiang, J. Zhang, N. Tsubaki, X. Li, Tuning interaction between cobalt catalysts and nitrogen dopants in carbon nanospheres to promote Fischer-Tropsch synthesis, Appl. Catal. B Environ. 248 (2019) 73–83, https://doi.org/10.1016/j.apcatb.2019.02.024.

[15] X. Pan, X. Bao, Reactions over catalysts confined in carbon nanotubes, Chem. Commun. (2008) 6271–6281, https://doi.org/10.1039/b810994j.

[16] L. Tang, C. Song, X. Yang, M. Li, B. Hu, Promotion of Mn Doped Co/CNTs Catalysts for CO Hydrogenation to Light Olefins, Chin. J. Chem. (2013) 826–830, https://doi.org/10.1002/cjoc.201300248.

[17] C. Tucker, E. van Steen, Effect of crystallite size distribution on the oxidation and re-reduction of cobalt in the Fischer–Tropsch synthesis: a thermodynamic analysis, Catal. Lett. 151 (2021) 2631–2637, https://doi.org/10.1007/s10562-020-03475-7.

[18] C.L. Tucker, M. Claeys, E. Van Steen, Decoupling the deactivation mechanisms of a cobalt Fischer-Tropsch catalyst operated at high conversion and "simulated" high conversion, Catal, Sci. Technol. 10 (2020) 7056–7066, https://doi.org/10.1039/d0cy00929f.

[19] A.M. Saib, D.J. Moodley, I.M. Ciobîc, M.M. Hauman, B.H. Sigwebela, C.J. Weststrate, J.W. Niemantsverdriet, J. Van De Loosdrecht, Fundamental understanding of deactivation and regeneration of cobalt Fischer-Tropsch synthesis catalysts, Catal. Today 154 (2010) 271–282, https://doi.org/10.1016/j.cattod.2010.02.008.

[20] B. Qiu, C. Yang, W. Guo, Y. Xu, Z. Liang, D. Ma, R. Zou, Highly dispersed Co-based Fischer – Tropsch. catalysts from metal-organic frameworks, J. Mater. Chem. A 74 (2017) 8081–8086, https://doi.org/10.1039/C7TA02128C.

[21] T. Fu, Z. Li, Review of recent development in Co-based catalysts supported on carbon materials for Fischer-Tropsch synthesis, Chem. Eng. Sci. 135 (2015) 3–20, https://doi.org/10.1016/j.ces.2015.03.007.

[22] R. Goyal, B. Sarkar, A. Bag, F. Lefebvre, S. Sameer, Single-step synthesis of hierarchical B_xCN : a metal- free catalyst for low-temperature oxidative dehydrogenation of propane, J. Mater. Chem. A (2016) 18559–18569, https://doi.org/10.1039/C6TA06972J.

[23] J. Wu, L. Wang, B. Lv, J. Chen, Facile Fabrication of BCN Nanosheet-Encapsulated Nano-Iron as Highly Stable Fischer-Tropsch Synthesis Catalyst, ACS Appl. Mater. Interfaces 9 (16) (2017) 14319–14327, https://doi.org/10.1021/acsami.7b00561.

[24] Y. Ide, F. Liu, J. Zhang, N. Kawamoto, K. Komaguchi, Y. Bando, D. Golberg, Hybridization of Au nanoparticle-loaded TiO_2 with BN nanosheets for efficient solar-driven photocatalysis, J. Mater. Chem. A 2 (2014) 4150–4156, https://doi.org/10.1039/c3ta13769d.

[25] W. Sun, Y. Meng, Q. Fu, F. Wang, G. Wang, W. Gao, X. Huang, F. Lu, High-yield production of boron nitride nanosheets and its uses as a catalyst support for hydrogenation of nitroaromatics, ACS Appl. Mater. Interfaces 8 (2016) 9881–9888, https://doi.org/10.1021/acsami.6b01008.

[26] Y.H. Zhang, K.G. Zhou, X.C. Gou, K.F. Xie, H.L. Zhang, Y. Peng, Effects of dopant and defect on the adsorption of carbon monoxide on graphitic boron nitride sheet: A first-principles study, Chem. Phys. Lett. 484 (2010) 266–270, https://doi.org/10.1016/j.cplett.2009.11.051.

[27] T. Cao, J. Feng, E.G. Wang, Adsorption of hydrogen on the interface of a graphene/boron nitride hybrid atomic membrane, Phys. Rev. B - Condens. Matter Mater. Phys. 84 (2011) 1–7, https://doi.org/10.1103/PhysRevB.84.205447.

[28] H. Zhao, H. Jiang, M. Cheng, Q. Lin, Y. Lv, Y. Xu, J. Xie, J. Liu, Z. Men, D. Ma, Boron adsorption and its effect on stability and CO activation of χ-Fe_5C_2 catalyst: an ab initio DFT study, Appl. Catal. A Gen. 627 (2021), 118382.

[29] J. Deng, M. Gao, J. Hasegawa, X. Zhang, A. Wang, A. Chen, D. Zhang, Unravelling the anomalous coking-resistance over boron nitride supported Ni catalysts for dry reforming of methane, CCS Chem. (2022) 1–41, https://doi.org/10.31635/ccschem.022.202202342.

[30] H. Wang, W. Zhou, J.X. Liu, R. Si, G. Sun, M.Q. Zhong, H.Y. Su, H.B. Zhao, J. A. Rodriguez, S.J. Pennycook, J.C. Idrobo, W.X. Li, Y. Kou, D. Ma, Platinum-modulated cobalt nanocatalysts for low-temperature aqueous-phase Fischer-Tropsch synthesis, J. Am. Chem. Soc. 135 (2013) 4149–4158, https://doi.org/10.1021/ja400771a.

[31] M. Ojeda, R. Nabar, A.U. Nilekar, A. Ishikawa, M. Mavrikakis, E. Iglesia, CO activation pathways and the mechanism of Fischer – Tropsch synthesis, J. Catal. 272 (2010) 287–297, https://doi.org/10.1016/j.jcat.2010.04.012.

[32] C.J. Bertole, C.A. Mims, G. Kiss, The effect of water on the Cobalt-Catalyzed Fischer – Tropsch Synthesis, J. Catal. 96 (2002) 84–96, https://doi.org/10.1006/jcat.2002.3666.

[33] J. Gahtori, G. Singh, C.L. Tucker, E. Van Steen, A.V. Biradar, A. Bordoloi, Insights into promoter-enhanced aqueous phase CO hydrogenation over Co@TiO₂ mesoporous nanocomposites, Fuel. (2021), 122402, https://doi.org/10.1016/j.fuel.2021.122402.

[34] J. Gahtori, C.L. Tucker, T.S. Khan, C. De, T. Rocha, A. Bordoloi, Highly efficient ZIF-67-derived PtCo alloy-CN interface for low- temperature aqueous-phase Fischer-Tropsch synthesis, Appl. Mater. Interfaces 14 (34) (2022) 38905–38920, https://doi.org/10.1021/acsami.2c11296.

[35] J. Gahtori, V. Kumar, T.S. Khan, M.A. Haider, S. Paul, A. Bordoloi, Dopant induced modification of support-surface structure for high throughput conversion of CO in aqueous media, Fuel. 326 (2022), 124961, https://doi.org/10.1016/j.fuel.2022.124961.

[36] S. Chen, P. Li, S. Xu, X. Pan, Q. Fu, X. Bao, Carbon doping of hexagonal boron nitride porous materials toward CO₂ capture, J. Mater. Chem. A 6 (2018) 1832–1839, https://doi.org/10.1039/c7ta08515j.

[37] S.J. Clark, M.D.S. Ii, C.J.P. Ii, P.J.H. Iii, M.I.J.P. Iv, K.R. Vi, First principles methods using CASTEP, Zeitschrift für Kristallographie - Crystalline Materials 220 (2005) 567–570, https://doi.org/10.1524/zkri.220.5.567.65075.

[38] J.P. Perdew, K. Burke, M. Ernzerhof, Generalized gradient approximation made simple, Phys. Rev. Lett. 77 (1996) 3865–3868, https://doi.org/10.1103/PhysRevLett.77.3865.

[39] Mater. Data C₃N₄ by Mater. Proj, 2022.

[40] C. Huang, C. Chen, X. Ye, W. Ye, J. Hu, C. Xu, X. Qiu, Stable colloidal boron nitride nanosheet dispersion and its potential application in catalysis, J. Mater. Chem. A 1 (2013) 12192–12197, https://doi.org/10.1039/c3ta12231j.

[41] F.A.J. Al-Doghachi, U. Rashid, Yun Hin Taufiq Yap, Investigation of Ce(iii) promoter effects on the tri-metallic Pt, Pd, Ni/MgO catalyst in dry-reforming of methane, RSC Adv. 6 (2016) 10372–10384, https://doi.org/10.1039/C5RA25869C.

[42] P. Muhammed Shafi, A. Chandra Bose, Impact of crystalline defects and size on X-ray line broadening: A phenomenological approach for tetragonal SnO₂ nanocrystals, AIP Adv. 5 (2015), https://doi.org/10.1063/1.4921452.

[43] S. Dong, X. Hao, X. Xu, D. Cui, M. Jiang, The effect of reactants on the benzene thermal synthesis of BN, Mater. Lett. 58 (2004) 2791–2794, https://doi.org/10.1016/j.matlet.2004.04.022.

[44] B. Singh, G. Kaur, P. Singh, K. Singh, B. Kumar, A. Vij, M. Kumar, R. Bala, R. Meena, A. Singh, A. Thakur, A. Kumar, Nanostructured boron nitride with high water dispersibility for boron neutron capture therapy, Sci. Rep. 6 (2016) 35535.

[45] D. Shi, B. Chang, Z. Ai, H. Jiang, F. Chen, Y. Shao, J. Shen, Y. Wu, X. Hao, Boron carbonitride with tunable B/N Lewis acid/base sites for enhanced electrocatalytic overall water splitting, Nanoscale. 13 (2021) 2849–2854, https://doi.org/10.1039/d0nr06857h.

[46] H. Mo Koo, X. Wang, A. Rong Kim, C.-H. Shin, J. Wook Bae, Effects of self-reduction of Co nanoparticles on mesoporous graphitic carbon-nitride to CO hydrogenation activity to hydrocarbons, Fuel. 287 (2021), 119437.

[47] H. Tabassum, C. Qu, K. Cai, W. Aftab, Z. Liang, T. Qiu, A. Mahmood, W. Meng, R. Zou, Large-scale fabrication of BCN nanotube architecture entangled on a three-dimensional carbon skeleton for energy storage, J. Mater. Chem. A 6 (2018) 21225–21230, https://doi.org/10.1039/C8TA08590K.

[48] D. Nabaho, J.W. Niemantsverdriet, M. Claeys, E. Van Steen, Hydrogen spillover in the Fischer-Tropsch synthesis: an analysis of platinum as a promoter for cobalt-alumina catalysts, Catal. Today 261 (2016) 17–27, https://doi.org/10.1016/j.cattod.2015.08.050.

[49] S.S. Liu, D.M. Luo, X. Yang, C.X. Tong, L.G. Tao, H.P. Ding, J. Zhang, Effect of g-C₃N₄ nano-structure on catalytic performance of CoOx/g-C₃N₄ in catalytic combustion of toluene, Int. J. Environ. Sci. Technol. 17 (2020) 3055–3064, https://doi.org/10.1007/s13762-020-02659-3.

[50] P. Patel, S. Nandi, M.S. Maru, R.I. Kureshy, N.H. Khan, Nitrogen-rich graphitic carbon stabilized cobalt nanoparticles as an effective heterogeneous catalyst for hydrogenation of CO₂ to formate, J. CO2 Util. 25 (2018) 310–314, https://doi.org/10.1016/j.jcou.2018.04.015.

[51] L. Chen, X. Tian, Y. Fu, J. Shen, The effect of surface acidic and basic properties of highly loaded Co catalysts on the Fischer-Tropsch synthesis, Catal. Commun. 28 (2012) 155–158, https://doi.org/10.1016/j.catcom.2012.09.009.

[52] S. Krishnamoorthy, M. Tu, M.P. Ojeda, D. Pinna, E. Iglesia, An Investigation of the Effects of Water on Rate and Selectivity for the Fischer – Tropsch Synthesis on Cobalt-based Catalysts, J. Catal. 433 (2002) 422–433, https://doi.org/10.1006/jcat.2002.3749.

[53] V. Sanchez-Escribano, M.A. Larrubia Vargas, E. Finocchio, G. Busca, On the mechanisms and the selectivity determining steps in syngas conversion over supported metal catalysts, Appl. Catal. A Gen. 316 (2007) 68–74, https://doi.org/10.1016/j.apcata.2006.09.020.

[54] K. Hadjiivanov, B. Tsyntsarski, T. Venkov, D. Klissurski, M. Daturi, J. Saussey, J. C. Lavalley, FTIR spectroscopic study of CO adsorption on Co-ZSM-5: evidence of formation of Co⁺(CO)₄ species, Phys. Chem. Chem. Phys. 5 (2003) 1695–1702, https://doi.org/10.1039/b300844d.

[55] D.D. Hibbitts, B.T. Loveless, M. Neurock, E. Iglesia, Mechanistic Role of Water on the Rate and Selectivity of Fischer-Tropsch Synthesis on Ruthenium Catalysts** Angewandte, 2013, pp. 12273–12278, https://doi.org/10.1002/anie.201304610.

[56] S. Storsater, O. Borg, E. Blekkan, A. Holmen, Study of the effect of water on Fischer–Tropsch synthesis over supported cobalt catalysts, J. Catal. 231 (2005) 405–419, https://doi.org/10.1016/j.jcat.2005.01.036.

[57] C.L. Tucker, E. van Steen, Activity and selectivity of a cobalt-based Fischer-Tropsch catalyst operating at high conversion for once-through biomass-to-liquid operation, Catal. Today 342 (2020) 115–123, https://doi.org/10.1016/j.cattod.2018.12.049.

[58] W. Ma, G. Jacobs, Y. Ji, T. Bhatelia, D.B. Bukur, S. Khalid, B.H. Davis, Fischer–Tropsch Synthesis: Influence of CO Conversion on Selectivities, H₂/CO Usage Ratios, and Catalyst Stability for a Ru Promoted Co/Al₂O₃ Catalyst Using a Slurry Phase Reactor, Top. Catal. 54 (2011) 757–767, https://doi.org/10.1007/s11244-011-9699-5.

[59] X. Lu, X. Zhu, C.M. Masuku, D. Hildebrandt, D. Glasser, A Study of the Fischer-Tropsch Synthesis in a batch Reactor: Rate, phase of Water, and Catalyst Oxidation, Energy Fuel 31 (2017) 7405–7412, https://doi.org/10.1021/acs.energyfuels.7b00624.